ARCTIC WILDFIRES

Unprecedented fire activity above the Arctic Circle linked to rising temperatures

Adrià Descals[1,2]*, David L. A. Gaveau[3], Aleixandre Verger[1,2,4], Douglas Sheil[5,6], Daisuke Naito[6,7], Josep Peñuelas[1,2]

Arctic fires can release large amounts of carbon from permafrost peatlands. Satellite observations reveal that fires burned ~4.7 million hectares in 2019 and 2020, accounting for 44% of the total burned area in the Siberian Arctic for the entire 1982–2020 period. The summer of 2020 was the warmest in four decades, with fires burning an unprecedentedly large area of carbon-rich soils. We show that factors of fire associated with temperature have increased in recent decades and identified a near-exponential relationship between these factors and annual burned area. Large fires in the Arctic are likely to recur with climatic warming before mid-century, because the temperature trend is reaching a threshold in which small increases in temperature are associated with exponential increases in the area burned.

Emissions from Arctic wildfires jeopardize global climate goals (*1*). The Arctic is warming rapidly because of a climate change–related phenomenon known as "Arctic amplification" (*2*); annual mean temperature has already increased more than 2°C compared with that of the preindustrial era (*3*) and is expected to reach 3.3° to 10°C above the 1985–2014 average by 2100 (*4*). These increased temperatures result in thawing of permafrost and deterioration of peatlands with emissions of carbon dioxide and methane (*5*–*7*). High-latitude peatlands are expected to become a net carbon source as a consequence of global warming (*8*). The release of carbon creates positive feedback with additional emissions contributing to further warming and thawing with further peatland degradation and emissions. In this context, the numerous fires identified by satellite thermal sensors in eastern Siberia in 2020 (*9*) raise particular concerns because of the resulting emissions (*10*).

Wildfires are common in the Arctic and Subarctic (*11*), but their size, frequency, and intensity are expected to increase as the climate warms (*12*). Extreme weather, such as that in 2020 in the Siberian Arctic (*13*), is expected to become more severe as Arctic oscillations weaken over time (*14*). Previous research in the Alaskan tundra suggests that the annual burned area might be two times greater than in the 1950–2010 period by the end of the century as warmer and drier conditions coincide more frequently (*15*). The conditions that affected the Arctic fire seasons of 2019 and 2020 in the Siberian Arctic have provided new empirical observations between climatic factors and burn extent and may already be indicating the changes in fire regimes expected by the end of the century. The fire seasons of 2019 and 2020, however, raised two uncertainties—first, whether the annual burned area above the Arctic Circle was actually increasing. Satellite-derived burned-area products tend to underestimate the true extent of burning (*12*), and rigorous validation techniques are required (*16*). Second, even if the burned areas in 2019 and 2020 were the largest yet observed, the links to other trends required evaluation.

We assessed annual burned area in the Siberian Arctic (latitudes >66.5°N) for 1982–2020 using six satellite-derived maps of burned areas (fig. S1). We investigated the Siberian Arctic because it is where most burning occurs above the Arctic Circle and fire frequency appeared to be increasing (*9*). We investigated 10 factors associated with the likelihood of fire: six climatic variables [air and surface temperature, total precipitation, wind speed and direction, and vapor-pressure deficit (VPD)], three variables describing the vegetation conditions [length of the growing season, mean normalized difference vegetation index ($NDVI_{mean}$), and climatic water deficit (CWD)], and the number of ignitions, a direct factor associated with the likelihood of fires. We evaluated how these factors have varied over the past four decades and their relationships with satellite-derived estimates of annual burned areas. Lastly, we investigated the future trends of annual burned area and fire emissions under future Representative Concentration Pathways (RCPs).

Results

Trends of burned area for 1982–2020

Between 1982 and 2020, the satellite burned-area products indicate that 12.97 million hectares (Mha) burned in the circumpolar region (latitudes >66.5°N). The Siberian Arctic, a region with continuous permafrost, accounted for 71% of this burned area. The years 2019 and 2020 had the greatest mapped burned area in Siberia above the Arctic Circle (Fig. 1A) (see supplementary text A for consistency of the time series of the burned area and fig. S2), which represents 44% of the total mapped burned area (9.24 Mha) in the region from 1982 to 2020. The burned area mapped in the Siberian Arctic varied between the satellite products, most notably the MCD64A1 product for 2019 and 2020 (Fig. 2A). The burned areas for 2020 were 1.71, 2.38, 2.59, and 2.62 Mha for MCD64A1, C3SBA10, Landsat, and Sentinel-2, respectively.

The sampling-based burned area in 2020, based on an assessment of errors of omission and commission (*16*), was nearly 3 Mha (MCD64A1 = 2.83 ± 0.26 Mha, C3SBA10 = 2.92 ± 0.17 Mha, Landsat = 2.92 ± 0.15 Mha, and Sentinel-2 = 2.99 ± 0.14 Mha) (see full assessment of accuracy in table S1 and a description of the results in supplementary Text B). The area estimate for 2019 and 2020 amounts to ~4.7 Mha. The mapped burned area is less than the estimated burned area for all four products because the omission errors of the "burned" class (ranging from 15.5 to 53.7%) are higher than the commission errors (ranging from 3.2 to 23.0%). Our estimates of carbon emissions from burning were 55.3 and 90.4 Tg C for 2019 and 2020, respectively, which is 156.7 and 256.1 Tg CO_2-eq (including CO_2 and CH_4) (fig. S3). Fires in 2020 damaged a wide area (0.71 Mha) of carbon-rich peatlands (organic carbon storage >20 kg C m^{-2}), indicated with a reference map of soil carbon storage (Fig. 1B) (*8*). The area of carbon-rich peatlands affected by fires has also recently expanded: 70% of total burned area occurred in these areas within the past 8 years of the record, and 30% occurred in 2020 (Fig. 2B).

Trends of the fire factors for 1982–2020

Various factors that may exacerbate the risk of fire have increased significantly over the past four decades in the Siberian Arctic (Fig. 3 and fig. S4). Air temperature, NDVI, the length of the growing season, and VPD have steadily risen. The average increase in summer air temperature was 0.66°C per decade. In 2019 and 2020, the mean summer air temperature was 11.35° and 11.53°C, which was 2.65° and 2.82°C higher than the 1982–2020 average, respectively. CWD, a proxy of plant water stress defined as the difference between potential and actual evapotranspiration, also increased between 1982 and 2020, although the linear trend likely began in the 2000s. More surprising, however, was the abrupt increase in CWD in 2019 and 2020. The estimated number of ignitions, total precipitation, and wind speed all had strong interannual variations, and the slope of their trends was not significantly different from zero.

[1]CREAF, Centre de Recerca Ecològica i Aplicacions Forestals, Cerdanyola del Vallès, 08193 Barcelona, Catalonia, Spain. [2]CSIC, Global Ecology Unit CREAF-CSIC-UAB, Bellaterra, 08193 Barcelona, Catalonia, Spain. [3]TheTreeMap; Bagadou Bas, 46600 Martel, France. [4]CIDE, CSIC-UV-GV, 46113 València, Spain. [5]Forest Ecology and Forest Management Group, Wageningen University and Research, Wageningen, Netherlands. [6]Center for International Forestry Research (CIFOR), Bogor 16000, Indonesia. [7]Graduate School of Agriculture, Kyoto University, Kitashirakawa Oiwake-cho, Sakyo-ku, Kyoto 606-8502, Japan.
*Corresponding author. Email: a.descals@creaf.uab.cat

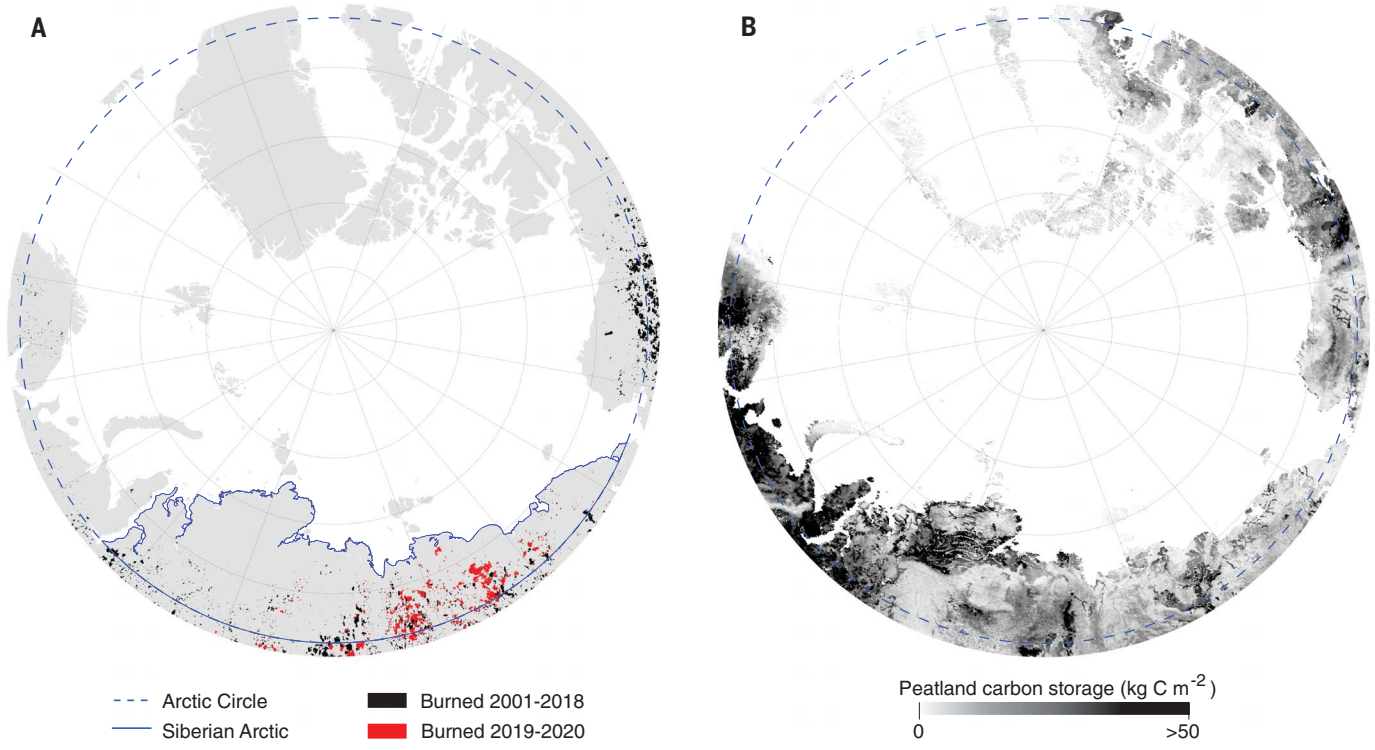

Fig. 1. Maps of burned area for 2001–2020 and peatland carbon storage in the circumpolar region. (**A**) Extent of the burns for 2001–2018 is from the FireCCI51 product, and the extent for 2019 and 2020 is the union of the C3SBA10 product and the Sentinel-2 burned-area map developed in this study. The Siberian Artic is the area inside the blue outline. Black represents areas that burned at least once for 2001–2018, and red represents areas that burned in 2019 and 2020. Areas that burned at least once in both periods, in 2001–2018 and 2019–2020, are also depicted in red; these areas represent only 3% of total burning above the Arctic Circle during the 2001–2020 period. We show the annual burned area from 2001 to 2020, which is the period when the occurrence of fires accelerated. (**B**) Estimated storage of organic carbon in peatlands from a reference dataset (*8*).

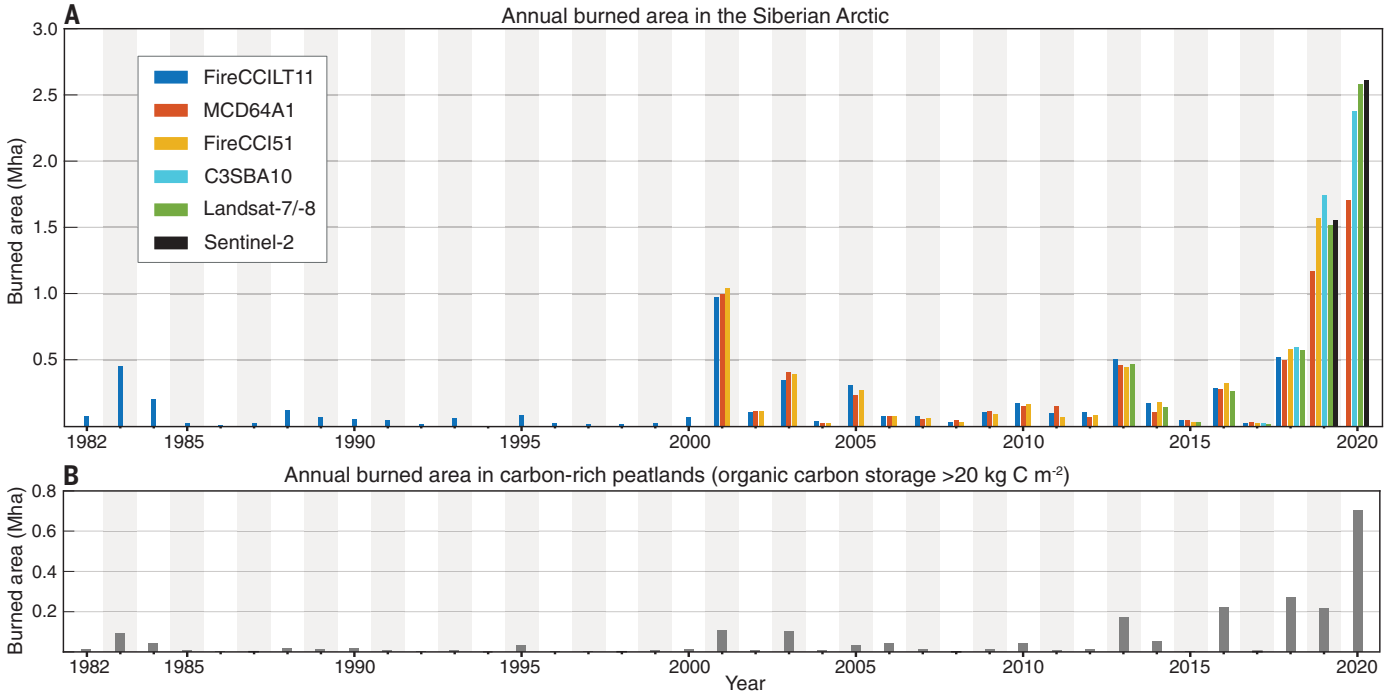

Fig. 2. Annual burned area in the Siberian Arctic and in carbon-rich peatlands for 1982–2020. (**A**) Annual burned area in the Siberian Arctic derived from remotely sensed data from six products. (**B**) Annual burned area in carbon-rich peatlands; >20 kg C m^{-2} in storage of organic carbon obtained from a reference dataset (*8*). The annual burned area in carbon-rich peatlands represents the median burned area for the available satellite products. Satellite burned-area products contain no data for 1994.

The annual number of detected ignitions was relatively consistent, with a median of 143, but high counts were observed in specific years, peaking at 423 in 2020. Seventy-two percent of these 2020 ignitions were detected within 20 days, between 13 June and 3 July, reaching Siberian Arctic regions as far north as 72.9° (fig. S5). Notably, these ignitions coincided with anomalously high values of convective available potential energy (CAPE) (fig. S6), an indicator of convective storms and lightning. Between 13 June and 3 July, satellite thermal sensors registered a rapid increase in the number of active fire detections, which accounts for 40.6% of all hot spots detected in 2020. By contrast, hot spots detected before 13 June represented only 1.1%. Similar peaks in the number of detected ignitions, preceding high

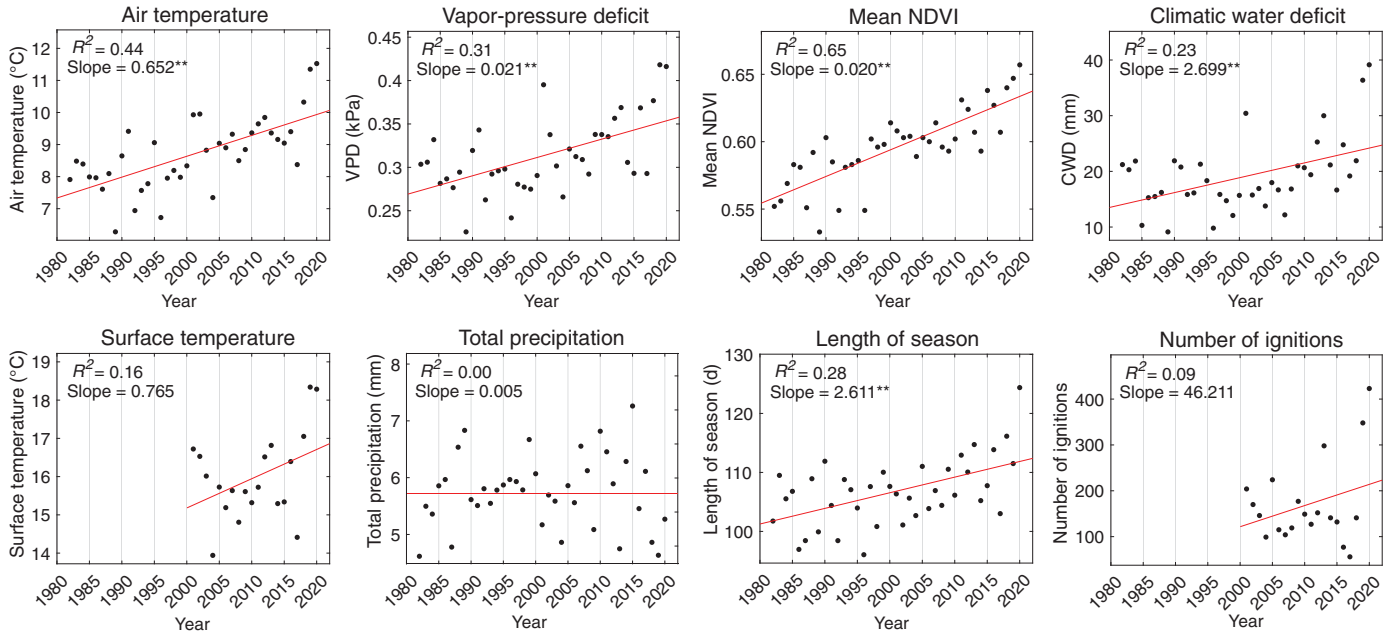

Fig. 3. Trends of eight fire factors in the Siberian Arctic during 1982–2020. Factors are the mean summer air and surface temperature, mean VPD, total summer precipitation, mean CWD, mean NDVI depicting vegetation green biomass, the length of the growing season, and the number of detected ignitions. The red lines are linear regressions; slopes are estimated on a decadal time scale. *p < 0.05; **p < 0.01.

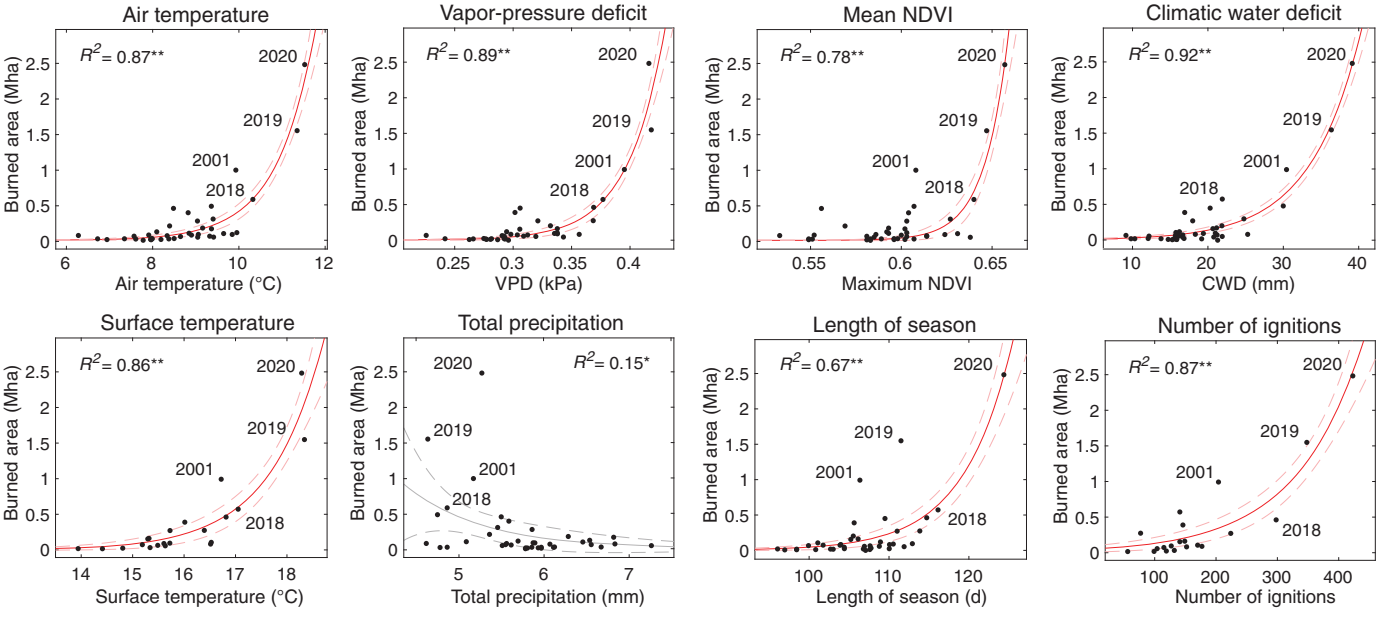

Fig. 4. Regression between the annual burned area and eight fire factors in the Siberian Arctic during 1982–2020. Solid lines are the best regression (linear or exponential), based on the coefficient of determination (R^2; *p < 0.05; **p < 0.01). The best regression model was the exponential for all the factors. The annual burned area is the median burned area for the available satellite products. The factors are the mean summer air and surface temperature, mean VPD, total precipitation, mean CWD, mean NDVI depicting green biomass, the length of the growing season, and the number of ignitions. Red solid lines depict a fit with a significant correlation (p < 0.01). The dashed lines are the 95% prediction limits of the regressions.

rates of active fire detection, occurred concurrently with high CAPE values in 2002, 2005, 2013, and 2018.

Sensitivity of the burned area to the fire factors

Linear and exponential regressions were used to analyze the best association between the annual burned area (aggregated with the median across available satellites for each year) and the factors of fire regime. An exponential regression was the best regression model (Fig. 4); the annual burned area accelerated when specific thresholds were exceeded. For example, the four years with the largest mapped burned areas (2001, 2018, 2019, and 2020) had a mean summer air temperature >10°C. The best fit was for CWD, which explained 92% of the interannual variability in the burned area. Other factors with a high coefficient of determination (R^2) were summer air temperature (87%), VPD (89%), and number of ignitions (87%). The annual burned area was correlated most weakly with total precipitation (15%). We also detrended the fire factors using the linear regression shown in Fig. 3 before determining the correlation with the annual burned area to reduce the potential of spurious correlations. The detrended correlations (fig. S7) confirmed the high R^2 for CWD (90%), air temperature (80%), VPD (51%), and number of ignitions (86%), but the correlation decreased for $NDVI_{mean}$ (from 78 to 11%).

We further examined the potential relationships among the fire-related factors in a structural equation modeling (SEM) (the rationale of the proposed relationships is described in the materials and methods). The hypothesized causal model outperformed the model validity analysis ($p > 0.05$ in the chi-square test; details on the covariances and residuals in the model are shown in table S2). The SEM supported the role of temperature in controlling other factors that affect the extent of burning (Fig. 5 and fig. S8). Temperature showed significant positive relationships with the lengthening of the growing season (0.66), the vegetation green biomass represented by $NDVI_{mean}$ (0.60), and atmospheric dryness measured by VPD (0.93). We hypothesized that these temperature-regulated factors and total precipitation would influence plant water stress, measured by CWD, but only VPD showed a significant effect (0.75) for the low number of observations ($n = 20$). Despite this, the hypothesized relationships displayed the expected sign. Temperature and CWD had a positive relationship with the number of detected ignitions (0.49 and 0.43, respectively). Annual burned area presented an R^2 of 0.82 and was directly explained by the number of detected ignitions (0.48) and the CWD (0.46).

Climate factors may differ locally and throughout the fire season. An additional analysis based on local weather conditions during the burning revealed that ignitions affecting areas larger than 4000 ha occurred with average hourly maximum temperatures of 28.6°C (SD = 3.4°C) and mean wind direction from the northeast (fig. S9). Thirty-day preignition precipitation was 0.37 mm (SD = 0.81 mm), and mean wind speed was 0.96 m s^{-1} (SD = 0.55 m s^{-1}). Ignitions that lead to burned areas larger than 4000 ha represent only 10% of all counts but account for 81% of all burned areas that were mapped between 2001 and 2020.

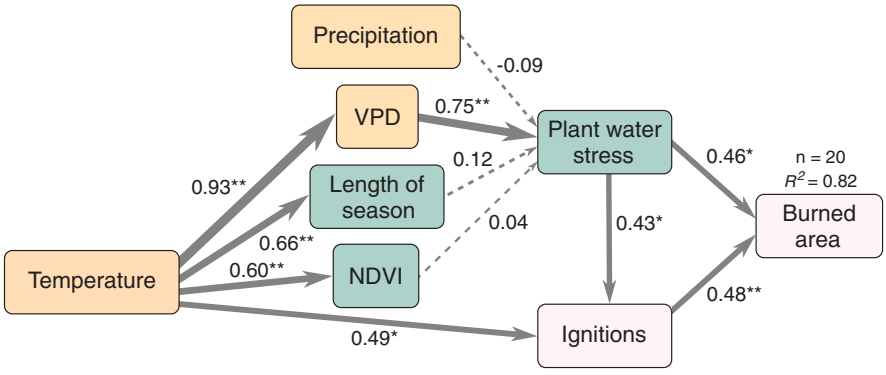

Fig. 5. Causality networks for the association among factors of fire in the Siberian Arctic for 2001–2020. Variables are categorized as climate (mean summer surface temperature, total precipitation, and mean VPD) (yellow), vegetation (mean summer NDVI depicting green biomass, the length of the growing season, and plant water stress measured by mean summer CWD) (green), and fire (number of detected ignitions and annual burned area) (light red). Factor loadings between variables are shown next to lines (*, $p < 0.05$; **$p < 0.01$). The width of the lines depicts the magnitude of the effect, and dashed lines represent nonsignificant effects. R^2 is the variance explained for the annual burned area.

Projections of annual burned area and carbon emissions under warming scenarios

Annual burned area in 2018, 2019, and 2020 more than doubled the long-term average, which was 0.24 Mha for the period 1982–2020 in the Siberian Arctic. Summer 2001, with a mean temperature nearing 10°C, was the first year on record to have a mapped burned area over twice that of the long-term average. The exponential regression between the burned area and temperature (Fig. 4) indicated that an annual burn of 0.5 Mha occurred at a mean summer temperature of 10.2°C. The 10°C threshold also indicated the rapid growth of the annual burned area in 2018, 2019, and 2020. This indicates that small increases in summer mean temperature above the 10°C threshold tend to be associated with extensive annual burned areas.

The linear trend of mean summer air temperature (Fig. 3) indicated that temperatures would reach 10.2°C by 2024 and reach the levels in 2020 by 2045 if mean summer temperatures continued to increase linearly at the current rate. (Fig. 6A). The RCP 4.5 and 8.5 scenarios also indicated an increase in temperatures that could substantially expand the burned area in the Siberian Arctic; annual burned area could range from 0.5 to 2.5 Mha before the middle of the century under RCP 4.5 and RCP 8.5 (Fig. 6B). This would result in a mean annual emission of 37.8 (SD = 14.4) Tg C $year^{-1}$ and 107.0 (SD = 40.7) Tg CO_2-eq $year^{-1}$ under RCP 8.5 between 2030 and 2050 (Fig. 6C), of which 27.6% would come from carbon-rich peatlands (Fig. 6D). Large fires of the magnitude observed in 2020 (burned area > 2.5 Mha) might recur on a yearly basis at the end of the century under RCP 8.5, with annual mean carbon emissions of 135.0 (SD = 69.0) Tg C $year^{-1}$ and 382.5 (SD = 195.6) Tg CO_2-eq $year^{-1}$ (27.9% from carbon-rich peatlands). Under the RCP 4.5 scenario, annual carbon emissions would stabilize [51.7 (SD = 18.8) Tg C $year^{-1}$] in the second half of the century, and fires such as those in 2020 (>2.5 Mha) would become less frequent in the Siberian Arctic, with a 10-year return interval if greenhouse gas concentrations stabilize by the middle of the century.

Discussion

The Siberian Arctic burned at the highest rates in 2019 and 2020, based on the burning trends over four decades of satellite data. Burning was sevenfold higher in 2020 than the 1982–2020 average and damaged an unprecedented area of peatlands. We found that temperature-related factors of fire regime have increased significantly over the past four decades and identified an exponential relationship between these factors and annual burned area, accounting for the unprecedented extent of the burns in 2019 and 2020.

The SEM results confirmed the positive association between higher temperatures, longer growing season, and greener vegetation. Higher temperatures account for the earlier snowmelt, permitting vegetation growth (*17*) and increased green biomass (*18*), which increases fuel availability. This earlier start of the growing season, also reported more widely (*19*),

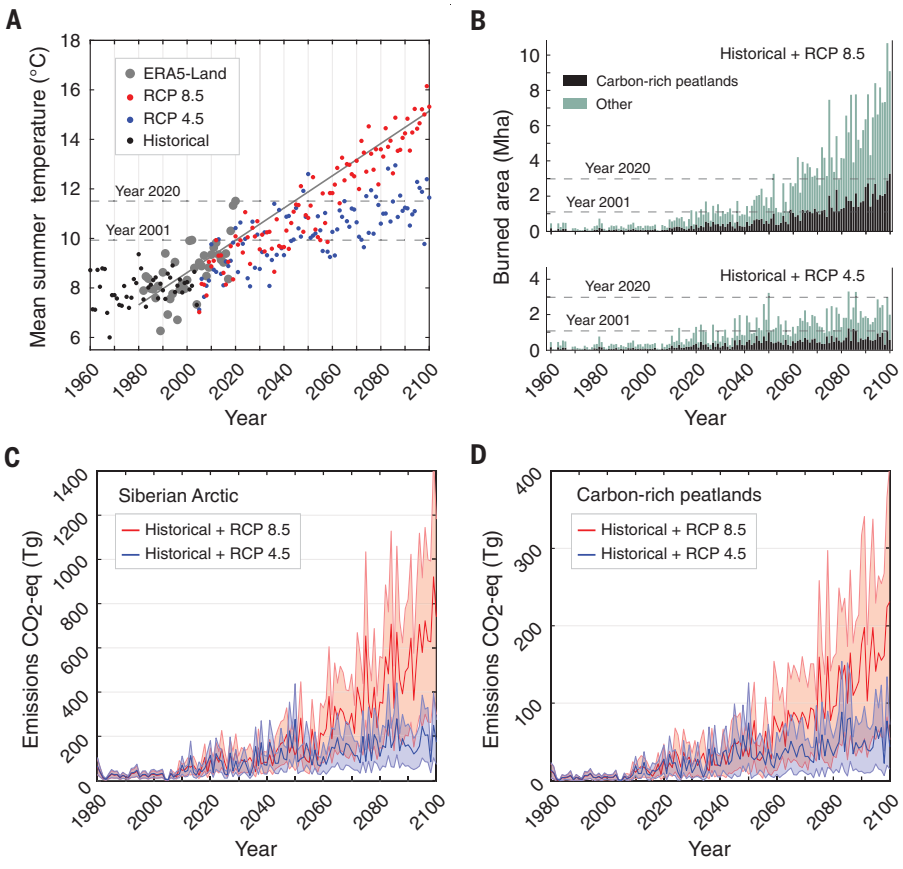

Fig. 6. Projected temperatures, annual burned areas, and emissions from fire in the Siberian Arctic. (**A**) Mean summer air temperatures from climate reanalysis (ERA-5 Land) during 1982–2020 and historical and projected temperatures under the RCP 4.5 and 8.5 scenarios based on HadGEM2-CC model. (**B**) Annual burned areas for the historical period and under the RCP 4.5 and 8.5 scenarios for carbon-rich peatlands (organic carbon storage >20 kg C m^{-2}) and other regions of the Siberian Arctic. (**C** and **D**) Projected CO_2-eq emissions under the RCP 4.5 and 8.5 in the Siberian Arctic (C) and carbon-rich soils (D).

modifies water use and availability such that plants may also experience water stress earlier in the season (*20*). According to the SEM results, the lengthening of the growing season and increasing green biomass of vegetation were associated with increased plant water stress, but the association was not significant, likely owing to the limited number of observations.

The increasing vulnerability to drought is exacerbated by extreme heatwaves, as in 2020, which can potentially desiccate plants and reduce moisture in peat and thus increase the severity of burning (*21*). This is reflected by the high influence of atmospheric dryness, measured by VPD, on plant water stress, represented by CWD, and its high correlation with annual burned area. Furthermore, CWD encompasses climatic factors, the water balance, and phenological changes that influence the susceptibility of vegetation to fire, so the interconnection of the fire factors with CWD may explain why CWD was best correlated with the annual burned area.

Climate warming and extreme weather may also account for the increase in the number of ignitions for specific years. The year 2020 had record-breaking temperatures and caused drought conditions early during the growing season (*13*). Recent warm winters, such as 2020, appear associated with abnormal circulation patterns that also favor the early spring snow melt and lower albedo that maintain warm conditions (*22*). Heatwaves and, more especially, increased surface temperatures are associated with convective storms and ignitions, as confirmed with the SEM. Whereas lightning remains infrequent at high latitudes, it is expected to increase as the climate warms (*23*). Climatic warming thus has a dual effect on fire regimes; warming increases the susceptibility of vegetation and peatlands to fire and increases the number of lightning-caused ignitions.

Increased winter warmth, as seen in 2020, reflects changes in circulation that draw more heat and moisture from lower latitudes (*24*). Circulation in eastern Siberia draws air and moisture from all directions of the compass (*25*) and is not immune to the so-called circulation "blocking" (*26*) seen elsewhere across the continent (*27*). Nonetheless, most burning occurs during relatively gentle winds blowing from the northeast, indicating that the processes that promote flammability may be distinct from those that promote the subsequent burning.

Our ignition detection method indicated that numerous fires started near simultaneously across a vast region during a period of atmospheric instability in the 2020 fire season, from which we speculate that lightning was the main cause of ignition, but local observations are required to verify this supposition. An alternative, or additional, explanation is that fires emerge from smoldering material that has persisted through the winter to reemerge when conditions permit a broader conflagration (*28*, *29*). We also found that satellite thermal sensors showed that fires spread quickly after high CAPE values and midseason ignitions, which suggests that most of the annual burned area is caused by fires that started during that time.

The link we see between fires and temperature suggests that severe fire years, such as 2020, will become increasingly common and resulting carbon emissions will rise. The magnitude of future fires and carbon emissions, however, remains uncertain. First, although the frequency of lightning strikes appears likely to increase as temperatures rise (*23*), the scale of any resulting fires depends on specific local weather and vegetation conditions, which remain challenging to predict. Second, we only considered direct emissions from burning and disregarded indirect emissions, although these are not necessarily negligible. Burning removes the peat that insulates permafrost, exposing it to thawing, which promotes soil respiration and the production of carbon dioxide and methane (*30*). Estimates from field studies in two different boreal forests in Alaska suggest that post-fire carbon emissions range from one-third to more than double those that occur during burning (*31*). Furthermore, permafrost prevents deeper burning in peatlands (*21*). As permafrost retreats, high temperatures and drying conditions may favor higher combustion rates (*32*). We used combustion rates ranging from 2.0 kg C m^{-2} for tundra to 3.4 kg C m^{-2} for boreal forests (*31*), but dry peatlands can release up to 16.8 kg C m^{-2} (*21*), indicating that much higher emissions are credible.

A previous study proposed temperature and rainfall thresholds for the annual burned areas in the Alaskan tundra (*15*). The extensive area burned in 2019 and 2020 corroborated the proposed curve-growth relationship between annual burned area and climate-related factors for the Alaskan tundra. Hu *et al.* (*15*) forecasted that the annual burned area would double in the Alaskan tundra by the end of the century. We found, however, that the annual burned area in the Siberian Arctic already doubled the long-term average in the past 3 years of the record. This increase in annual burned

area suggests that the Arctic is already experiencing a change in fire regimes caused by climatic warming. The burned areas in 2019 and 2020 might be exceptional occurrences, but the recent temperature trend and projected scenarios indicate that temperatures are reaching a threshold in which small increases above 10°C can alter fire-related factors and result in exponentially increasing burned area and associated fire emissions in the next decades. Forthcoming fires can potentially affect peatlands and deteriorate the permafrost, which in turn will exacerbate the carbon emissions from carbon-rich soils.

REFERENCES AND NOTES

1. S. M. Natali *et al*., *Proc. Natl. Acad. Sci. U.S.A.* **118**, e2100163118 (2021).
2. M. C. Serreze, J. A. Francis, *Clim. Change* **76**, 241–264 (2006).
3. E. Post *et al*., *Sci. Adv.* **5**, eaaw9883 (2019).
4. Arctic Monitoring and Assessment Programme, *Arctic Climate Change Update 2021: Key Trends and Impacts. Summary for Policy-Makers* (Arctic Monitoring and Assessment Programme, 2021).
5. E. A. Schuur *et al*., *Nature* **520**, 171–179 (2015).
6. K. Dutta, E. Schuur, J. Neff, S. Zimov, *Glob. Change Biol.* **12**, 2336–2351 (2006).
7. M. R. Turetsky *et al*., *Nat. Geosci.* **13**, 138–143 (2020).
8. G. Hugelius *et al*., *Proc. Natl. Acad. Sci. U.S.A.* **117**, 20438–20446 (2020).
9. A. Witze, *Nature* **585**, 336–337 (2020).
10. M. C. Mack *et al*., *Nature* **475**, 489–492 (2011).
11. N. H. French *et al*., *Int. J. Wildland Fire* **24**, 1045–1061 (2015).
12. J. L. McCarty *et al*., *Biogeosciences* **18**, 5053–5083 (2021).
13. A. Ciavarella *et al*., *Clim. Change* **166**, 9 (2021).
14. O. V. Churakova Sidorova, R. T. W. Siegwolf, M. V. Fonti, E. A. Vaganov, M. Saurer, *Sci. Rep.* **11**, 19010 (2021).
15. F. S. Hu *et al*., *Front. Ecol. Environ.* **13**, 369–377 (2015).
16. P. Olofsson *et al*., *Remote Sens. Environ.* **148**, 42–57 (2014).
17. A. Descals *et al*., *Sci. Total Environ.* **742**, 140637 (2020).
18. L. T. Berner *et al*., *Nat. Commun.* **11**, 4621 (2020).
19. S. Piao *et al*., *Glob. Chang. Biol.* **25**, 1922–1940 (2019).
20. J. Peñuelas, T. Rutishauser, I. Filella, *Science* **324**, 887–888 (2009).
21. M. R. Turetsky, W. F. Donahue, B. W. Benscoter, *Nat. Commun.* **2**, 514 (2011).
22. A. B. M. Collow *et al*., *J. Clim.* **35**, 3075–3090 (2022).
23. Y. Chen *et al*., *Nat. Clim. Chang.* **11**, 404–410 (2021).
24. Q. You *et al*., *Earth Sci. Rev.* **217**, 103625 (2021).
25. J. Piao, W. Chen, S. Chen, H. Gong, Q. Zhang, *J. Clim.* **33**, 3883–3899 (2020).
26. C. You, M. Tjernström, A. Devasthale, D. Steinfeld, *Geophys. Res. Lett.* **49**, e2022GL097899 (2022).
27. T. Nakamura, T. Sato, *Environ. Res.* **209**, 112881 (2022).
28. R. C. Scholten, R. Jandt, E. A. Miller, B. M. Rogers, S. Veraverbeke, *Nature* **593**, 399–404 (2021).
29. J. L. McCarty, T. E. Smith, M. R. Turetsky, *Nat. Geosci.* **13**, 658–660 (2020).
30. J. E. Holloway *et al*., *Permafr. Periglac. Process.* **31**, 371–382 (2020).
31. S. Veraverbeke *et al*., *Curr. Opin. Environ. Sci. Health* **23**, 100277 (2021).
32. M. R. Turetsky *et al*., *Nat. Geosci.* **8**, 11–14 (2015).
33. A. Descals, adriadescals/ArcticFires: Arctic Fire repository, *Zenodo* (2022). https://doi.org/10.5281/zenodo.6907765.
34. E. Chuvieco, M. L. Pettinari, G. Otón, ESA Fire Climate Change Initiative, (Fire_cci): AVHRR-LTDR Burned Area Grid product, Centre for Environmental Data Analysis, Version 1.1 (2020). http://dx.doi.org/10.5285/62866635ab074e07b93f17fbf87a2c1a
35. L. Giglio, C. Justice, L. Boschetti, D. Roy, MCD64A1 MODros. Inf. Serv./Terra+ aqua burned area monthly L3 global 500m SIN grid V006, NASA EOSDIS. Inf. Serv. Land Processes DAAC (2015). https://doi.org/10.5067/MODIS/MCD64A1.006.
36. E. Chuvieco, M. Pettinari, J. Lizundia-Loiola, T. Storm, M. Padilla Parellada, ESA Fire Climate Change Initiative, (Fire_cci): MODros. Inf. Serv. Fire_cci burned area pixel product, Centre for Environmental Data Analysis, version 5.1 (2018). https://doi.org/10.5285/58f00d8814064b79a0c49662ad3af537.
37. Copernicus Climate Change Service, Fire burned area from 2001 to present derived from satellite observations, Copernicus Climate Change Service (C3S) Climate Data Store (CDS) (2019). https://doi.org/10.24381/cds.f333cf85.
38. Z. Wan, S. Hook, G. Hulley, MOD11A2 MODIS/Terra land surface temperature/emissivity 8-day L3 global 1km SIN grid V006, NASA EOSDIS Land Processes DAAC (2015). https://doi.org/10.5067/MODIS/MOD11A2.006.
39. J. Muñoz Sabater, ERA5-Land monthly averaged data from 1950 to present, Copernicus Climate Change Service (C3S) Climate Data Store (CDS) (2019). https://doi.org/10.24381/cds.68d2bb30.
40. J. T. Abatzoglou, S. Z. Dobrowski, S. A. Parks, K. C. Hegewisch, Monthly climate and climatic water balance for global terrestrial surfaces from 1958-2015, University of Idaho (2017). ttps://doi.org/10.7923/G43J3B0R.
41. H. Wouters, J. Berckmans, R. Maes, E. Vanuytrecht, K. De Ridder, Global bioclimatic indicators from 1950 to 2100 derived from climate projections, Copernicus Climate Change Service (C3S) Climate Data Store (CDS) (2021). https://doi.org/10.24381/cds.a37fecb7.
42. K. Didan, MOD13Q1 MODIS/Terra vegetation indices 16-day L3 global 250m SIN grid V006, NASA EOSDIS. Inf. Serv. Land Processes DAAC (2015). https://doi.org/10.5067/MODIS/MOD13Q1.006.

ACKNOWLEDGMENTS

Funding: This work was funded by the Ministry of Agriculture, Forestry and Fisheries (MAFF) of the government of Japan and the Center for International Forestry Research ("CIFOR"), through the project "Transitions to Climate Resilient Landscapes: Reducing and Mitigating Boreal and Tropical Forest Fires to Promote Sustainable Rural Livelihoods." We acknowledge funds from the Spanish Government grant PID2019-110521GB-I00, the Fundación Ramón Areces grant CIVP20A6621, and the Catalan Government grant SGR 2017-1005. This work represents a contribution to CSIC PTI-TELEDETECT. **Author contributions:** Conceptualization: A.D., D.L.A.G., and J.P. Methodology: A.D. and D.L.A.G. Investigation: A.D. and D.L.A.G. Visualization: A.D., D.L.A.G., and J.P. Supervision: J.P. Writing – original draft: A.D. and D.L.A.G. Writing – review and editing: A.D., D.L.A.G., A.V., D.S., D.N., and J.P. **Competing interests:** Authors declare that they have no competing interests. **Data and materials availability:** All source code and the Sentinel-2 and Landsat-8 burned-area maps are available at Zenodo (*33*). Other data that support the findings of the study are openly available. The burned area time series derived from AVHRR sensors (FireCCILT11) (*34*) is available at https://doi.org/10.5285/62866635ab074e07b93f17fbf87a2c1a. The burned area time series derived from MODIS sensors are available at https://doi.org/10.5067/MODIS/MCD64A1.006 for the MCD64A1 product (*35*) and https://doi.org/10.5285/58f00d8814064b79a0c49662ad3af537 for the FireCCI51 (*36*) product. The burned area time series derived from Sentinel-3 (C3SBA10) (*37*) is available at https://doi.org/10.24381/cds.f333cf85. The Landsat-7 and -8 surface reflectance datasets are available at https://earthexplorer.usgs.gov, and the Sentinel-2 Level-2A surface reflectance at https://scihub.copernicus.eu. The active fire datasets obtained from MODIS is available at https://firms.modaps.eosdis.nasa.gov/active_fire. Fire emission datasets were downloaded from the FIRECAM platform https://globalfires.earthengine.app/view/firecam. Land surface temperature from MODIS (MOD11A2) (*38*) is available at https://doi.org/10.5067/MODIS/MOD11A2.006. Climate reanalysis ERA5-Land Monthly (*39*) is available at https://doi.org/10.24381/cds.68d2bb30, and TERRACLIMATE dataset (*40*) is available at https://doi.org/10.7923/G43J3B0R. The downscaled air temperature projections from the HadGEM2-CC model (*41*) are available at https://doi.org/10.24381/cds.a37fecb7. The storage of organic carbon from peatlands is available at https://bolin.su.se/data/hugelius-2020. Lastly, the NDVI time series from the GIMMS3g dataset is available at https://www.nasa.gov/nex/data, and the NDVI from the MOD13Q1v6 product (*42*) at https://doi.org/10.5067/MODIS/MOD13Q1.006.

SUPPLEMENTARY MATERIALS

science.org/doi/10.1126/science.abn9768
Materials and Methods
Supplementary Text
Figs. S1 to S9
Tables S1 and S2
References (*43*–*65*)

Submitted 7 January 2022; accepted 13 September 2022
10.1126/science.abn9768